High Frequency Nonlinear Response of Superconducting Cavity-Grade Nb surfaces

Bakhrom Oripov,[1, *] Thomas Bieler,[2] Gianluigi Ciovati,[3] Sergio Calatroni,[4] Pashupati Dhakal,[3] Tobias Junginger,[5] Oleg B. Malyshev,[6] Giovanni Terenziani,[4] Anne-Marie Valente-Feliciano,[3] Reza Valizadeh,[6] Stuart Wilde,[6] and Steven M. Anlage[1]

[1] *Center for Nanophysics and Advanced Materials, Department of Physics, University of Maryland, College Park, MD 20742, USA*
[2] *Chemical Engineering and Materials Science, Michigan State University, East Lansing, Michigan 48824, USA*
[3] *Thomas Jefferson National Accelerator Facility, Newport News, Virginia 23606, USA*
[4] *European Organization for Nuclear Research (CERN), 1211 Geneva 23, Switzerland*
[5] *Engineering Department, Lancaster University, Lancaster LA1 4YW, United Kingdom*
[6] *ASTeC, STFC Daresbury Laboratory, Warrington WA4 4AD, United Kingdom*
(Dated: June 14, 2019)

Nb superconducting radio-frequency (SRF) cavities are observed to break down and lose their high-Q superconducting properties at accelerating gradients below the limits imposed by theory. The microscopic origins of SRF cavity breakdown are still a matter of some debate. To investigate these microscopic issues, temperature- and power-dependent local third-harmonic response is measured on bulk Nb and Nb thin-film samples using a novel near-field magnetic microwave microscope between 2.9 and 10 K and 2 and 6 GHz. Both periodic and nonperiodic response as a function of applied rf field amplitude are observed. We attribute these features to extrinsic and intrinsic nonlinear responses of the sample. The rf-current-biased resistively shunted junction (RSJ) model can account for the periodic response and fits very well to the data using reasonable parameters. The nonperiodic response is consistent with vortex semiloops penetrating into the bulk of the sample once sufficiently high rf magnetic field is applied and the data can be fit to a time-dependent Ginzburg-Landau (TDGL) model of this process. The fact that these responses are measured on a wide variety of Nb samples suggests that we are capturing the generic nonlinear response of air-exposed Nb surfaces.

I. INTRODUCTION

Researchers studying high-energy physics are considering several next-generation accelerator designs, including the International Linear Collider (ILC), where a very large number (approximately 16000) of Nb superconducting radio-frequency (SRF) cavities will be employed [1, 2]. Each cell works under high rf fields with the highest electric field on the accelerating axis and the maximum magnetic field on the equator of the cylindrical cavity [3].

The high-accelerating gradient performance of Nb SRF cavities is often limited by breakdown events below the intrinsic limiting surface fields of Nb. These breakdowns are often caused by defects at discrete locations inside the cavity [4, 5]. Although cavities with high-quality surfaces with excellent rf properties had been achieved, there is a lack of detailed understanding of the causal links among surface treatments, defects, and ultimate rf performance at low temperatures with many theoretical models being proposed to address the issue [6–9]. Cavity uniformity will be one of the key requirements of the ILC; thus, the ability to mass produce high-quality SRF cavities and diagnose them rapidly is very important.

Lately, various optical and other inspection techniques for finished cavities have been developed. For example a temperature map of the cavity exterior is taken and hot spots are identified [10, 11]. Then a high-resolution optical image of the cavity interior is taken and pits and other defects are identified [5, 12]. Later, the correlation between defects and hot spots is studied. As an example, a

theory that describes the relation between the breakdown field and the geometry of surface pits has been developed [13]. Currently, studies that focus on elemental composition and purity of material [14], dc critical magnetic field or superheating field [15], postmortem microanalysis of hot-cold spots [16],[17] or various sophisticated optical inspection tools [5, 12] make up the backbone of SRF material science. These efforts have resulted in advancements in cavity treatment recipes that have led to SRF cavities with high gradients and high-quality factors $> 3 \times 10^{10}$ at 1.3 GHz and 2K. However, it is not possible to locally and directly probe rf performance of the active interior surface of a cavity at low temperatures.

Finally, there is also interest in looking beyond Nb to superconductors like MgB_2 and other superconductor coatings or the possibility of reducing the cost by using Nb-coated copper cavities. There is also a proposal to create superconductor/insulator multilayer thin-film coatings with enhanced rf critical fields [18]. However, often it is very costly and/or difficult to build full-size SRF cavities with high-quality versions of these new materials to see if they really are superior. Hence there is a need to quantitatively examine these materials at high frequencies and low temperatures using simpler methods that effectively reproduce the demanding conditions found operating in SRF cavities.

Based on the needs of the SRF community, we successfully build a near-field magnetic microwave microscope using a magnetic writer from a conventional magnetic
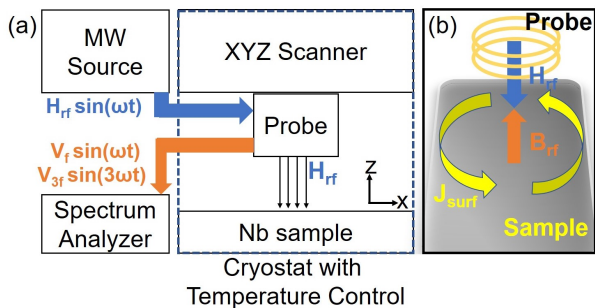
FIG. 1. (a) Schematic of experimental setup. A microwave (MW) source is used to generate rf signal and feed it to the magnetic probe. The sample response magnetic field is coupled back to the probe and measured with a spectrum analyzer. (b) Sketch of the probe-sample interaction. The magnetic probe is approximated as a current loop producing perpendicular magnetic field inducing screening currents on the surface of the sample. This current generates a response magnetic field that is coupled back to the same probe.

recording hard-disk drive [19–24]. This microscope is capable of locally measuring both linear and nonlinear rf response. The nonlinear response is far more sensitive to applied rf power than the linear response [25] and it can be linked to the nonlinear surface impedance of the sample [26], which is an important parameter for a SRF cavity driven by high rf magnetic field. Furthermore, surface defects are expected to locally suppress the rf critical current, which leads to a higher nonlinear response, thus making this microscope an excellent defect detector [27, 28].

II. EXPERIMENTAL SETUP

The magnetic write head inside a conventional hard disk-drive is a true engineering marvel. Nearly 1000 processing steps are needed to fabricate one [29], but once finished a write head can produce $B_{RF} \approx 600\text{-}mT$ rf magnetic field localized to an approximately 100-nm length scale [30]. In this experiment, a Seagate perpendicular magnetic writer head is attached to a cryogenic XYZ positioner and used in a scanning probe fashion. Electrical contacts are made by directly soldering SMA coaxial connectors to the pads on the end of the writer probe transmission line (see Fig. S1 in the Supplemental Material [31–37]). Probe characterization results and other details can be found in [21–24]. A microwave source is connected to the probe by coaxial cables (Fig. 1(a)). The probe is in contact with the sample, which is located on the cold plate of an Entropy 4K L-series cryostat with a base temperature of 2.8K. The probe produces a rf magnetic field perpendicular to the sample surface. The sample is in the superconducting state, so to maintain the Meissner state, a screening current is induced on the surface(Fig. 1(b)). This current generates a response magnetic field that is coupled back to the same probe, creates a propagating signal on the attached transmission line structure, and is measured with a spectrum an-

alyzer at room temperature. Since superconductors are intrinsically nonlinear [38], both linear and nonlinear responses to an applied rf magnetic field are expected. To improve the signal-to-noise ratio, stray nonlinear signals produced by the amplifiers and the spectrum analyzer itself have to be suppressed. For example, high pass filters are installed between the probe and spectrum analyzer in order to block the fundamental input frequency signal from reaching the spectrum analyzer and producing nonlinear signals [19–24]. Measurements are performed at a fixed input frequency while the temperature of the sample and applied rf field amplitude are varied. No external dc magnetic field is applied. The entire setup is shielded from external magnetic field by a cylindrical superconducting shield installed around the coldest enclosure of the cryostat.

The present microscope is an upgrade of an older-generation setup reported in Refs. [21–24]. The newer-generation magnetic write heads are able to induce stronger and more localized rf magnetic fields on the sample. A new cryogen-free cryostat enables collection of more data and detailed examination of a wide variety of bulk and thin- film Nb samples from different sample growers.

III. DATA

First, a bulk Nb sample provided by the Bieler group (MSU) originating from a Tokyo-Denkai large-grain Nb single crystal is examined. The surface of the sample is mechanically polished and then electropolished. Later, the sample is strained to 40% elongation, cut in half, and two differently oriented halves (F and C) are welded back together [24, 39]. The sample is then measured for a third-harmonic response at a fixed position on side C of the sample 4 mm away from the weld. This location experiences a brief thermal excursion that retains much of the deformed dislocation defect structure as described in more detail in Fig. 16 of Ref. [39] and Ref. [40].

Fig. 2 shows a plot of measured third-harmonic response (V_{3f}) vs temperature (T) and applied rf field amplitude (H_{rf}) at an $f = 4.38\text{-}GHz$ input frequency. A temperature-independent probe background is subtracted from the data for clarity. One notes several families of nonlinear response (separated by white and black dashed lines) that are roughly periodic as a function of applied rf amplitude.

Fig. 3 shows a vertical line cut through this image (V_{3f} vs H_{rf}) at a constant temperature of $T = 9.0K$. As shown in the figure, H_{p1}, H_{p2} and H_{p3} are the rf field amplitudes corresponding to the first three dips in $V_{3f}(H_{rf})$. At all temperatures, V_{3f} is periodic as a function of H_{rf} above a temperature-dependent onset amplitude $H_{p0}(T)$. There is no temperature-dependent V_{3f} signal above $9.3K$, indicating that the superconducting sample is indeed the source of the signal. To compare the temperature dependence of the dips, a temperature-
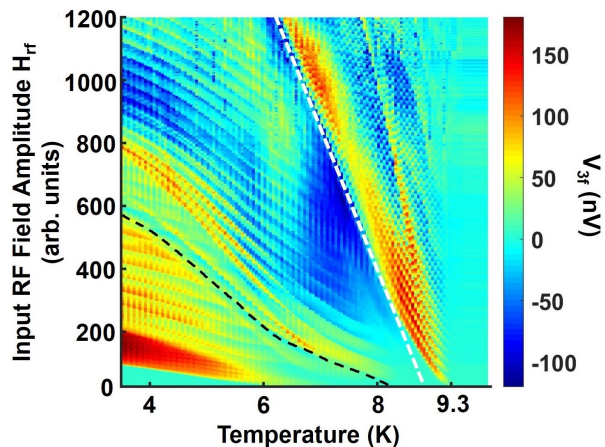
FIG. 2. (Color online) Third-harmonic voltage V_{3f} data vs temperature and applied rf field amplitude from a large-grain bulk Nb measured at a 4.38-GHz rf input frequency. A temperature-independent probe background nonlinearity has been subtracted, resulting in some negative values of V_{3f}.
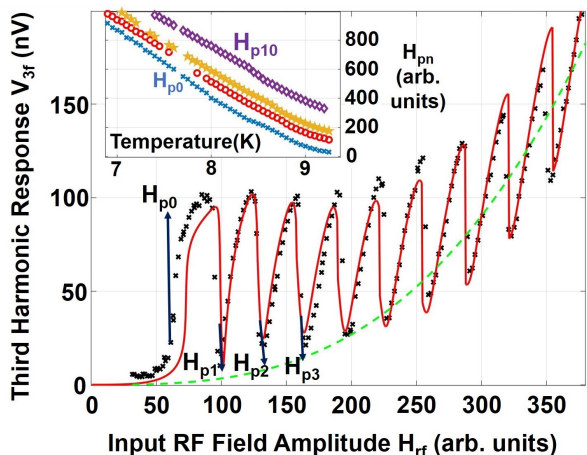

FIG. 3. (Color online) Bulk Nb data at T=9.0K (black $\times$ markers), probe background (green dashed line) and RSJ fit with $I_cR = 49.4\mu V$ (red solid line). Inset: H_{p0} (blue $\times$), H_{p3} (red circle), H_{p5} (orange $\star$) and H_{p10} (purple $\diamond$) vs temperature (K) from the data shown in Fig. 2.

dependent "period" and onset of periodicity $H_{p0}(T)$ are defined. At a constant temperature T, all dips $H_{pn}(T)$, where n stands for the n'th dip, are fit to a straight line as a function of n. The slope of the line is defined as "period" and the y-intercept is defined as the onset of periodicity $H_{p0}(T)$ (Fig. S3 in [31]). The inset of Fig. 3 shows the temperature dependence of $H_{p0}(T)$, $H_{p3}(T)$, $H_{p5}(T)$ and $H_{p10}(T)$. Fig. 2 shows several families of similar features, each with a different onset of periodicity H_{p0}, period and onset temperature, suggesting that several nonlinear sources are within the field of view of the probe.

Also, a thin-film sample is prepared at CERN by depositing Nb on a copper substrate by high-power impulse magnetron sputtering (HIPIMS). The plasma is driven
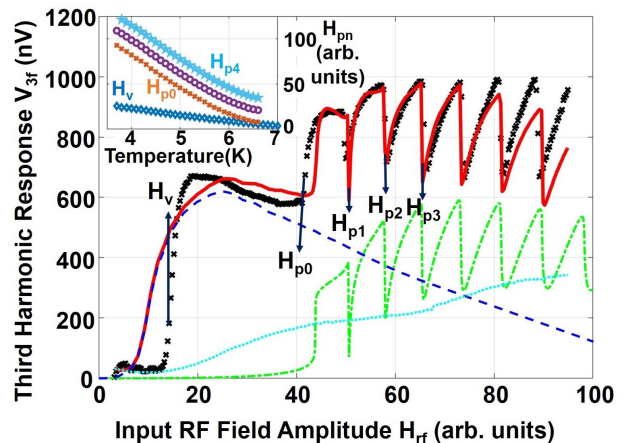

FIG. 4. (Color online) Third-harmonic response V_{3f} data at T=5.1K and 2.2 GHz on a Nb on Cu film sample from CERN (black $\times$ markers). Also shown are the RSJ fit with $I_cR = 58.3\mu V$ (green dashed-dotted line), time-dependent Ginzburg-Landau fit with $H_{dp} = 12$ (blue dashed line), probe background (cyan dotted line) and complete fit obtained by vector complex addition (red solid line). Inset: H_{p0} (red $\times$), H_{p2} (purple circle), H_{p4} (cyan $\star$) and onset of nonlinearity H_v (blue $\diamond$) vs temperature (K).

with rectangular voltage pulses in a frequency range of $50 - 500 Hz$ and pulse duration range of $50 - 200 \mu s$. The peak discharge current density is kept in the range of $0.2 - 1 A/cm^2$. This sample is well characterized by point-contact tunneling spectroscopy, low-energy muon spin rotation, and SEM. The point-contact tunneling measurements revealed that the sample has a distribution of superconducting gap values with a peak at $\Delta = 1.48 meV$ [41]. However, the tunneling data also show a few points with large zero-bias conductance peaks. The sample has a fine-grain structure with 50-100-nm average grain size [42]. Fig. 4 shows the measured V_{3f} vs H_{rf} at $T = 5.1K$ and 2.2 GHz rf input frequency. Similar to the bulk Nb sample, it also has a periodic response as a function of driving rf amplitude. However, the onset of periodicity H_{p0} is different from the onset of nonlinear response H_v. The inset shows the temperature dependence of $H_{p0}(T)$, $H_{p2}(T)$, $H_{p4}(T)$, and $H_v(T)$. Clearly, H_{p0} and H_v have different temperature dependencies, but the $H_{pn}(T)$ temperature dependencies are similar to those seen on the bulk Nb samples.

Measurements are performed on several other bulk Nb and Nb film samples and a very similar periodic response of V_{3f} vs H_{rf} is observed, showing that this is a generic response of this material (Figs. 6-8 in the Appendix). Overall, two types of nonlinear response are observed: a low-field nonperiodic and a higher-field periodic response. All Nb samples show either periodic or low-field response, or both, depending on the spatial location of the magnetic writer probe on the surface of the sample.

IV. MODELS

The oxidation of Nb when exposed to air is a well-known and complex phenomenon [43–46]. Oxygen forms a solid solution in Nb and produces materials with a continuous range of transition temperatures below the bulk T_c of pure Nb. A thin Nb-oxide layer on the surface of Nb sandwiched with a Nb superconductor on both sides can create a superconductor-insulator-superconductor (S-I-S) or superconductor-normal-metal-superconductor (S-N-S) Josephson junction [24]. Many theoretical works modeling linear and nonlinear rf impedance of weak-link Josephson junctions were previously published [47–51]. Experimental data showing the rf response of a weak-link Josephson junction in a high-temperature superconductor is also available [19, 47, 52].

In our experiment, the probe induces rf current on the surface of the sample. This current can bias a junction at or near the surface. The Josephson junction (JJ) is modeled as an ideal short junction shunted by a resistance (R) and a capacitance (C) to form a parallel circuit [49]. For a small driving frequency compared to the plasma frequency $\omega_p = \sqrt{\dfrac{2\pi I_c}{\Phi_0 C}}$ of the junction, the model can be simplified and the capacitive branch can be ignored. Here I_c is the critical current of the junction and Φ_0 is the magnetic flux quantum. The simplified circuit equation becomes $I_c \sin\delta + \dfrac{\Phi_0}{2\pi R}\dfrac{\partial \delta}{\partial t} = I_\omega \sin(\omega t)$, where δ is the gauge-invariant phase difference on the JJ, $V = \dfrac{\Phi_0}{2\pi}\dfrac{d\delta}{dt}$ is the potential difference across the junction and $I_\omega \sin(\omega t)$ is the rf current bias. In general, the voltage drop on the junction is nonsinusoidal in time and contains harmonics and subharmonics of the driving frequency ω. One can calculate third-harmonic voltage $V_{3\omega}$ across the junction as a function of driving current amplitude I_ω for a given critical voltage of the junction $I_c R$. The result closely resembles the experimental data (see the red solid line in Fig. 3, green dashed-dotted line in Fig. 4, and Fig. S4 in [31]). Each subsequent peak in $V_{3\omega}$ corresponds to an additional 2π phase slip across the junction in each rf cycle.

For the current-biased resistively shunted junction (RSJ) model, the onset-to-period ratio uniquely and monotonically depends on $I_c R$ (Fig. S5 inset in [31]). Thus the measured onset-to-period ratio from the data taken at a constant temperature allows direct extraction of $I_c R(T)$ for the junction. In turn $I_c R(T)$ can be used to calculate the superconducting gap $\Delta(T)$, and $\Delta(0)$ can be obtained from a BCS temperature dependence fit to $\Delta(T)$ (Fig. S6 in [31]). Note that the onset-to-period ratio provides a direct link between experimental data and numerical calculations from the model, and that the measured voltages are across the pads of the writer head, whereas the calculated voltages are across the junction.

Sample	Weak-link Family	$\Delta(0)$ (meV)	$T_c(K)$
Bulk Nb from MSU	1	0.80	9.28
	2	0.35	8.41
	3	0.33	7.28
Nb on Cu from CERN	1	0.25	6.76

TABLE I. Summary of fit superconducting gap and T_c values obtained from $I_c R(T)$ extracted from third-harmonic data on two Nb samples. Weak-link number indicates the family number in the data.
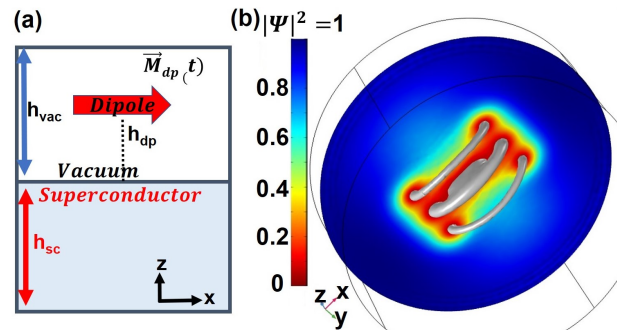

FIG. 5. (Color online) (a) Schematic TDGL simulation setup. The magnetic probe is approximated as a point magnetic dipole parallel to the surface. The simulation is divided into two domains: superconductor and vacuum. (b) Superconducting order parameter $|\Psi|^2$ evaluated at the superconductor surface at time $t = 73\tau_0$ looking from inside the superconducting domain into the vacuum domain. The dipole magnetic moment $\vec{M}_{dp}(t)$ is chosen such that the applied rf magnetic field at the surface of the superconductor below the dipole $\vec{B}(t) = 0.75\sin(\omega t)\hat{x}$. Grey contours represent surfaces of $|\Psi|^2 = 5 \times 10^{-3}$ and show three vortex semiloops penetrating inside the superconductor.

Thus, the RSJ fit plots in both Fig. 3 and Fig. 4 involve unknown scaling factors for both the rf amplitude and third-harmonic response.

Superconducting gap values obtained from fits shown in Table.I are lower than the bulk value $\Delta(0) = 1.55 meV$ reported elsewhere [53]. Nb samples with higher oxygen content tend to have lower superconducting gap values [43, 54]. Thus the superconducting gap value at a $Nb/NbO_x/Nb$ weak-link can be lower due to a gradient in oxygen content.

Note that three families of periodic features are visible in Fig. 2, with different periods and onsets H_{p0}. Table.I summarizes fits to these features as well as those on a thin-film sample. The fact that the responses from the weak-links have different superconducting gap $\Delta(0)$ values and T_c's shows that they likely have different oxygen content.

Even in the absence of defects, a superconductor subjected to a strong rf magnetic field can generate a nonlinear rf response [7]. This scenario is modeled by solving the time-dependent Ginzburg-Landau (TDGL) equa-

tions with COMSOL simulation software. The magnetic writer probe was approximated to be a pointlike magnetic dipole with a sinusoidal time-dependent magnetic moment $\vec{M}_{dp}(t)$, located at a height h_{dp} above the origin and parallel to the surface. The simulation is divided into two domains: superconductor: $-h_{sc} < z < 0$, and vacuum $0 < z < h_{vac}$ (see Fig.5.(a)). The TDGL equations are solved in the 1st domain while only Maxwell's equations are solved in the second domain with appropriate boundary conditions at the interface.

Fig. 5.(b) shows a snapshot of a typical TDGL simulation. As $\vec{M}_{dp}(t)$ of the dipole increases, a domain with a suppressed order parameter forms in the superconductor in a region below the dipole. Later in the rf cycle, as the magnetic field peaks and begins to decrease in magnitude the domain vanishes and vortex semiloops emerge (Fig. S9 in [31]). The response rf magnetic field is calculated from the time-dependent screening currents and the third-harmonic response recovered at the location of the dipole is obtained through Fourier transformation.

The TDGL-derived third-harmonic voltage $V_{3\omega}$ as a function of the peak magnetic moment of the dipole shows the following behavior. $V_{3\omega}$ is small for small moments but increases rapidly above an onset magnetic moment value corresponding to an onset rf field amplitude H_v at the surface, reaches a peak value and then slowly decreases back to a small finite value (see the blue long-dashed line in Fig.4). Note that this evolution is very similar to the low-field response, an example of which is shown in Fig.4 (the $H_{rf} < H_{p0}$ part of the data).

In total the data shown in Fig.4 have contributions from a nonlinear response generated by the current-biased junction, intrinsic low-field nonlinearity modeled by TDGL, and a temperature-independent probe background. First the onset-to-period ratio is calculated from the data. Then the I_cR value corresponding to the onset-to-period ratio of the data is found (Fig. S5 in [31]). Next, the horizontal axis scaling factor for the RSJ model is fixed to match the H_{p0} from the RSJ model to the H_{p0} from the data. Finally, complex vector addition of all three contributions is performed for a full fit (Fig. 4). The probe background was measured at 10K, which is above the T_c of Nb. The phase of the probe background was assumed to be constant and is set to zero, while the complex values of the model responses are included in the sum. The horizontal and vertical axis scaling factors for the TDGL model and the vertical axis scaling factor for the RSJ model are the three fitting parameters.

An estimate of the applied rf field strength created by the probe on the surface of the sample can be made as follows. At higher temperatures as $T \to T_c$, the upper critical magnetic field is given by $B_{c2}(T) \approx 2B_{c2}(0)(1 - T/T_c)$. By determining the H_{rf} value at which the periodic nonlinear response is suppressed, and assuming $B_{c2}(0) = 240mT$ [3, 55] and $T_c = 9.3K$, we can estimate the rf field experienced by the defect

to be $11.4\mu T/(arb.unit)$. This approximately calibrates the vertical axis in Fig. 2 and the horizontal axis in Fig. 3. Similarly, using the horizontal scaling factor of $< X_{scale} > = 0.22\mu V/(arb.units)$ obtained in the Supplemental Material [31] for weak-link 1 in Fig. 2 and an estimated weak-link normal state resistance of $R_n = 100\Omega$ [24], we can estimate the driving current flowing through the weak-link to be $2.2nA/(arb.unit)$. Thus, for weak-link 1 in Fig. 2, this would correspond to a maximum rf magnetic field amplitude of $13.7mT$ and maximum driving current of $I_\omega = 2.6\mu A$ with a zero-temperature critical current of $I_c(0) = 12.6\mu A$.

V. DISCUSSION

We measure a variety of Nb samples intended for SRF applications from five different sources (see the Appendix). A similar nonlinear response is observed in all of them. The intrinsic low-field nonlinear response calculated based on the GinzburgLandau (GL) model near T_c has a strong dependence on the sample thickness [22, 27]. Therefore, bulk Nb samples tend to have a weaker intrinsic nonlinear response compared to thin-film Nb samples. Depending on the spatial location of the probe, we observe a nonlinear response, which can be considered as a low-field response, a periodic response, or a combination of both. The response is also reproducible and the same result is obtained on a bulk large-grain Nb sample after an interval of 2 weeks, for example.

Note that the magnetic field created by the magnetic writer probe is very "aggressive" and introduces a perpendicular component; hence, it does not precisely replicate the parallel rf magnetic fields experienced inside a SRF cavity. Nevertheless, this method is a very useful tool to compare rf responses across a variety of samples and to identify the source of the nonlinearity. We can locate the weak-link, measure its superconducting gap, and compare local rf vortex nucleation fields H_v on the surface of superconducting samples.

In summary, we observe two generic types of local nonlinear response on the surfaces of air-exposed Nb bulk and thin-films. The nonlinear response is quantitatively modeled and understood. The existence of weak-links on air-exposed SRF grade Nb samples is experimentally confirmed. We also demonstrate the ability to successfully differentiate between the sources of local nonlinearity based on their dependence on rf field amplitude and temperature.
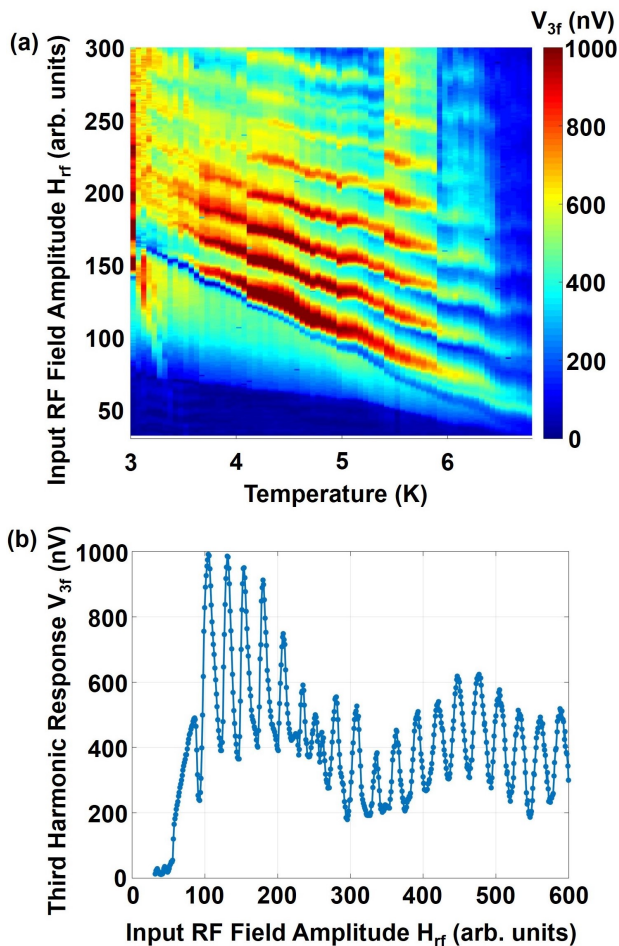
FIG. 6. (a) Small-grain bulk Nb third-harmonic data vs temperature and applied rf field amplitude measured at 5.07 GHz rf input frequency. The sample is provided by G. Ciovati at Jefferson Lab. (b) Vertical line cut through this image (V_{3f} vs H_{rf}) at a constant temperature of T=5.0 K.

FIG. 7. Third-harmonic response V_{3f} vs input rf field amplitude H_{rf} data at 7.5K and 4.855 GHz rf input frequency on Nb on Cu. The sample is provided by Oleg Malyshev's group in ASTeC.

APPENDIX: DATA FROM OTHER NB SAMPLES

Another set of bulk Nb samples is provided by the Ciovati group at Jefferson Lab. A high-purity fine-grain niobium sheet is cut into small samples by wire electrodischarge machining. Later, these samples are etched using buffered chemical polishing, heat treated at 600°C, and etched again. Afterward, the samples are nanopolished to obtain a surface with mirror-quality smoothness. Further details of sample preparation and characterization are available in ref. [56]. The data from this sample are very similar to the data obtained from large-grain bulk Nb sample. Fig.6 shows representative nonlinear response data from sample F9 mentioned in [56].
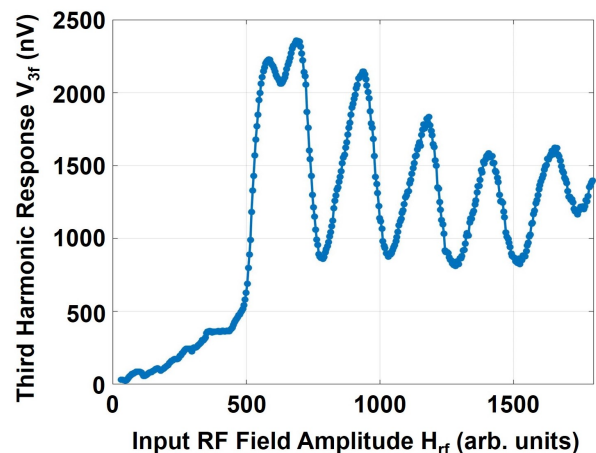
A set of Nb on copper thin-film samples is provided by the Malyshev group at the Accelerator Science and Technology Centre (ASTeC). Four samples are deposited by high-power impulse magnetron sputtering at 700°C and various bias voltages on the Cu substrate [57]. The plasma is driven with rectangular voltage pulses at a $200Hz$ frequency and $100\mu s$ pulse duration. The peak discharge current for each pulse is approximately $40A$. All Nb film depositions are continued for 4 hours and the resulting films have a thickness of $1.4\mu m$. The residual resistivity ratio (RRR) is measured to be in the $42-54$ range, peaking for the film prepared at 0 bias voltage. Fig.7 shows representative nonlinear response data from one of those samples. A periodic response of V_{3f} vs H_{rf} is observed, similar to the other samples.

A set of Nb thin-films is provided by the Valente-Feliciano group at Jefferson Lab. The sample is coated using energetic condensation deposition in UHV via an electron cyclotron resonance (ECR) Nb ion source with a continuous ion energy of 184 eV [55]. The sample has a thickness of 570 nm and is deposited on an Al_2O_3 substrate. The critical temperature is measured to be $T_c = 9.18K$ and the RRR is 31. Fig. 8 shows the representative nonlinear response data from this sample. In this case, fifth-harmonic response V_{5f} is measured and a very similar periodic response of V_{5f} vs H_{rf} is observed. A similar behavior of V_{5f} is observed in the CERN film. We find that the driven RSJ model shows dips in V_{5f} at the same H_{rf} as V_{3f}.

The data from all these samples are very similar to those in Figs. 2,3 and 4 in the main text. The fact that such a wide variety of Nb samples produce a similar response indicates that this is a generic response of air-exposed Nb surfaces.
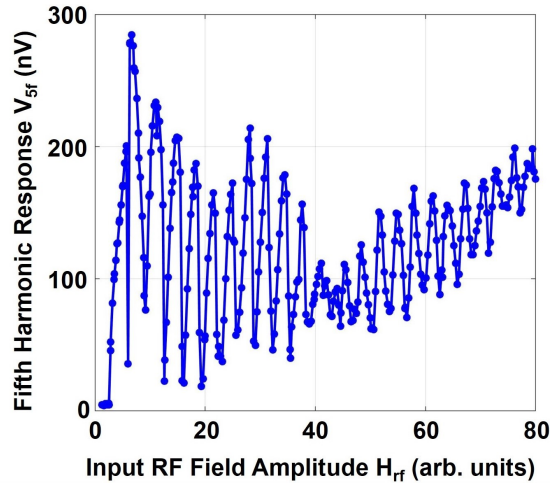
FIG. 8. Fifth-harmonic response V_{5f} vs input rf field amplitude H_{rf} data at 4.2K and 1.361 GHz rf input frequency on Nb thin-film. The sample is provided by A. Valente-Feliciano's group at Jefferson Lab.

[1] "International Linear Collider reference design report vol 3: Accelerator p 157," `http://ilcdoc.linearcollider.org/record/6321/files/ILC_RDR_Volume_3-Accelerator.pdf` (2007), accessed: 2019-03-01.

[2] "International linear collider website," `https://ilchome.web.cern.ch/ilc/facts-and-figures`, accessed: 2019-03-01.

[3] B. Aune, R. Bandelmann, D. Bloess, B. Bonin, A. Bosotti, M. Champion, C. Crawford, G. Deppe, B. Dwersteg, D. A. Edwards, H. T. Edwards, M. Ferrario, M. Fouaidy, P.-D. Gall, A. Gamp, A. Gössel, J. Graber, D. Hubert, M. Hüning, M. Juillard, T. Junquera, H. Kaiser, G. Kreps, M. Kuchnir, R. Lange, M. Leenen, M. Liepe, L. Lilje, A. Matheisen, W.-D. Möller, A. Mosnier, H. Padamsee, C. Pagani, M. Pekeler, H.-B. Peters, O. Peters, D. Proch, K. Rehlich, D. Reschke, H. Safa, T. Schilcher, P. Schmüser, J. Sekutowicz, S. Simrock, W. Singer, M. Tigner, D. Trines, K. Twarowski, G. Weichert, J. Weisend, J. Wojtkiewicz, S. Wolff, and K. Zapfe, "Superconducting TESLA cavities," Phys. Rev. ST Accel. Beams **3**, 092001 (2000).

[4] M Ge, G Wu, D Burk, J Ozelis, E Harms, D Sergatskov, D Hicks, and L D Cooley, "Routine characterization of 3D profiles of SRF cavity defects using replica techniques," Superconductor Science and Technology **24**, 035002 (2010).

[5] Yoshihisa Iwashita, Yujiro Tajima, and Hitoshi Hayano, "Development of high resolution camera for observations of superconducting cavities," Phys. Rev. ST Accel. Beams **11**, 093501 (2008).

[6] A. Gurevich, "Multiscale mechanisms of SRF breakdown," Physica C: Superconductivity **441**, 38 – 43 (2006).

[7] A. Gurevich and G. Ciovati, "Dynamics of vortex penetration, jumpwise instabilities, and nonlinear surface resistance of type-II superconductors in strong RF fields," Phys. Rev. B **77**, 104501 (2008).

[8] A. Romanenko and D. I. Schuster, "Understanding quality factor degradation in superconducting niobium cavities at low microwave field amplitudes," Phys. Rev. Lett. **119**, 264801 (2017).

[9] Alex Gurevich, "Theory of RF superconductivity for resonant cavities," Superconductor Science and Technology **30**, 034004 (2017).

[10] Jens Knobloch, Henry Muller, and Hasan Padamsee, "Design of a high speed, high resolution thermometry system for 1.5 GHz superconducting radio frequency cavities," Review of Scientific Instruments **65**, 3521–3527 (1994).

[11] A. Canabal, J. D. Bowyer, P. Chacon, N. A. Gillespie, M. A. Madrid, and T. Tajima, "Development of a temperature mapping system for 1.3-ghz 9-cell srf cavities," in *2007 IEEE Particle Accelerator Conference (PAC)* (2007) pp. 2406–2408.

[12] K Watanabe, "Review of optical inspection methods and results," in *Proceedings, 14th International Conference on RF Superconductivity (SRF 2009): Berlin, Germany, Sept 20-25, 2009* (SRF2009) p. TUOBAU01.

[13] Takayuki Kubo, "Magnetic field enhancement at a pit on the surface of a superconducting accelerating cavity," Progress of Theoretical and Experimental Physics **2015**, 073G01 (2015).

[14] H. Safa, D. Moffat, B. Bonin, and F. Koechlin, "Advances in the purification of niobium by solid state gettering with titanium," Journal of Alloys and Compounds **232**, 281 – 288 (1996).

[15] Oleg Malyshev, Keith Dumbell, Alexander Gurevich, Lewis Gurran, Ninad Pattalwar, Shrikant Pattalwar, and Reza Valizadeh, "First Results of Magnetic Field Penetration Measurements on Multilayer S-I-S Structures," in *Proceedings 7th International Particle Accelerator Conference (IPAC 2016): Busan, Korea, May 8-13, 2016*, p. WEPMB057, doi: 10.18429/JACoW-IPAC2016-WEPMB057.

[16] Xin Zhao, G. Ciovati, and T. R. Bieler, "Characterization of etch pits found on a large-grain bulk niobium superconducting radio-frequency resonant cavity," Phys. Rev. ST Accel. Beams **13**, 124701 (2010).

[17] Y. Trenikhina, A. Romanenko, J. Kwon, J.-M. Zuo, and J. F. Zasadzinski, "Nanostructural features degrading the performance of superconducting radio frequency niobium cavities revealed by transmission electron microscopy and electron energy loss spectroscopy," Journal of Applied Physics **117**, 154507 (2015).

[18] A. Gurevich, "Enhancement of RF breakdown field of superconductors by multilayer coating," Applied Physics Letters **88**, 012511 (2006).

[19] Sheng-Chiang Lee, Su-Young Lee, and Steven M. Anlage, "Microwave nonlinearities of an isolated long $YBa_2Cu_3O_{7-\delta}$ bicrystal grain boundary," Phys. Rev. B **72**, 024527 (2005).

[20] Dragos I. Mircea, Hua Xu, and Steven M. Anlage, "Phase-sensitive harmonic measurements of microwave nonlinearities in cuprate thin films," Phys. Rev. B **80**, 144505 (2009).

[21] T. Tai, X. X. Xi, C. G. Zhuang, D. I. Mircea, and S. M. Anlage, "Nonlinear near-field microwave microscope for RF defect localization in superconductors," IEEE Transactions on Applied Superconductivity **21**,

2615–2618 (2011).

[22] T. Tai, B. G. Ghamsari, and S. M. Anlage, "Nanoscale electrodynamic response of Nb superconductors," IEEE Transactions on Applied Superconductivity **23**, 7100104–7100104 (2013).

[23] Tamin Tai, Behnood G. Ghamsari, Thomas R. Bieler, Teng Tan, X. X. Xi, and Steven M. Anlage, "Near-field microwave magnetic nanoscopy of superconducting radio frequency cavity materials," Applied Physics Letters **104**, 232603 (2014).

[24] Tamin Tai, B. G. Ghamsari, T. Bieler, and Steven M. Anlage, "Nanoscale nonlinear radio frequency properties of bulk nb: Origins of extrinsic nonlinear effects," Phys. Rev. B **92**, 134513 (2015).

[25] D. E. Oates, Y. D. Agassi, and B. H. Moeckly, "Intermodulation distortion and nonlinearity in MgB_2: Experiment and theory," IEEE Transactions on Applied Superconductivity **17**, 2871–2874 (2007).

[26] D. E. Oates, "Overview of nonlinearity in HTS: What learned and prospects for improvement," Journal of Superconductivity and Novel Magnetism **20**, 3–12 (2007).

[27] Sheng-Chiang Lee, Mathew Sullivan, Gregory R. Ruchti, Steven M. Anlage, Benjamin S. Palmer, B. Maiorov, and E. Osquiguil, "Doping-dependent nonlinear meissner effect and spontaneous currents in high-T_c superconductors," Phys. Rev. B **71**, 014507 (2005).

[28] J. C. Booth, L. R. Vale, and R. H. Ono, "On-wafer measurements of nonlinear effects in high temperature superconductors," IEEE Transactions on Applied Superconductivity **11**, 1387–1391 (2001).

[29] Barry Stipe., "The magnetic hard disk drive - how information is stored in the cloud," (Presented at the annual APS March Meeting 2018, Los Angeles, CA, March 5-9 2018, available online at `https://www.youtube.com/watch?v=faUZZLSwdKA`).

[30] Michael J. Conover, principal engineer at Seagate Technology, "modeled magnetic field contours-private communication," January 29, 2018.

[31] For further details on experimental results and theoretical models, see Supplemental Material at `https://arxiv.org/src/1904.07432/anc/Supplemental_Material.pdf`.

[32] Michael Tinkham, *Introduction to superconductivity*, 2nd ed. (Dover Publications, Inc., Mineola, New York, 2004) Chap. 3, p. 63.

[33] M Cyrot, "Ginzburg-Landau theory for superconductors," Reports on Progress in Physics **36**, 103–158 (1973).

[34] I. S. Aranson, N. B. Kopnin, and V. M. Vinokur, "Dynamics of vortex nucleation by rapid thermal quench," Phys. Rev. B **63**, 184501 (2001).

[35] Tommy Sonne Alstrøm, Mads Peter Sørensen, Niels Falsig Pedersen, and Søren Madsen, "Magnetic flux lines in complex geometry Type-II superconductors studied by the Time Dependent Ginzburg-Landau equation," Acta Applicandae Mathematicae **115**, 63–74 (2011).

[36] William D. Gropp, Hans G. Kaper, Gary K. Leaf, David M. Levine, Mario Palumbo, and Valerii M. Vinokur, "Numerical simulation of vortex dynamics in Type-II superconductors," Journal of Computational Physics **123**, 254 – 266 (1996).

[37] Tamin Tai, *Measuring Electromagnetic Properties of Superconductors in High and Localized RF Magnetic Field*, Ph.D. thesis, University of Maryland (2013), available at https://drum.lib.umd.edu/handle/1903/14668.

[38] D. Xu, S. K. Yip, and J. A. Sauls, "Nonlinear Meissner effect in unconventional superconductors," Phys. Rev. B **51**, 16233–16253 (1995).

[39] T. R. Bieler, N. T. Wright, F. Pourboghrat, C. Compton, K. T. Hartwig, D. Baars, A. Zamiri, S. Chandrasekaran, P. Darbandi, H. Jiang, E. Skoug, S. Balachandran, G. E. Ice, and W. Liu, "Physical and mechanical metallurgy of high purity Nb for accelerator cavities," Phys. Rev. ST Accel. Beams **13**, 031002 (2010).

[40] Derek Baars, *Investigation of active slip systems in high purity single crystal Nb*, Ph.D. thesis, Michigan State University (2013), page 110, available at https://publications.nscl.msu.edu/thesis/Baars_2013_410.pdf.

[41] Tobias Junginger, S Calatroni, A Sublet, G Terenziani, T Prokscha, Z Salman, A Suter, T Proslier, and J Zasadzinski, "A low energy muon spin rotation and point contact tunneling study of niobium films prepared for superconducting cavities," Superconductor Science and Technology **30**, 125013 (2017), doi: 10.1088/1361-6668/aa8926.

[42] Giovanni Terenziani, Sergio Calatroni, and Arutiun Ehiasarian, "Niobium Coatings for Superconducting RF Applications by HIPIMS," in *Proceedings 4th International Conference on Fundamentals and Industrial Applications of HIPIMS: Braunschweig, Germany, June 10-13, 2013*, p. 16, doi: 10.13140/2.1.2837.9846.

[43] J. Halbritter, "On the oxidation and on the superconductivity of niobium," Applied Physics A **43**, 1–28 (1987).

[44] J. Halbritter, "Transport in superconducting niobium films for radio frequency applications," Journal of Applied Physics **97**, 083904 (2005).

[45] Kevin E. Yoon, David N. Seidman, Claire Antoine, and Pierre Bauer, "Atomic-scale chemical analyses of niobium oxide/niobium interfaces via atom-probe tomography," Applied Physics Letters **93**, 132502 (2008).

[46] C. Nico, T. Monteiro, and M.P.F. Graa, "Niobium oxides and niobates physical properties: Review and prospects," Progress in Materials Science **80**, 1 – 37 (2016).

[47] Alan M. Portis, *Electrodynamics of High-Temperature Superconductors* (World Scientific, Singapore, 1993).

[48] L. M. Xie, J. Wosik, and J. C. Wolfe, "Nonlinear microwave absorption in weak-link Josephson junctions," Phys. Rev. B **54**, 15494–15499 (1996).

[49] J. McDonald and John R. Clem, "Microwave response and surface impedance of weak links," Phys. Rev. B **56**, 14723–14732 (1997).

[50] Z. Zhai, Patanjali V. Parimi, and S. Sridhar, "Nonlinear microwave impedance of short and long Josephson junctions," Phys. Rev. B **59**, 9573–9580 (1999).

[51] A. Sheikhzada and A. Gurevich, "Nonlinear dynamics of Josephson vortices in a film screen under dc and ac magnetic fields," Physica C: Superconductivity and its Applications **506**, 59 – 68 (2014).

[52] H. Xin, D. E. Oates, S. Sridhar, G. Dresselhaus, and M. S. Dresselhaus, "Observation of individual josephson vortices in $YBa_2Cu_3O_{7-\delta}$ bicrystal grain-boundary junctions," Phys. Rev. B **61**, R14952–R14955 (2000).

[53] T. Proslier, J. F. Zasadzinski, L. Cooley, C. Antoine, J. Moore, J. Norem, M. Pellin, and K. E. Gray, "Tunneling study of cavity grade Nb: Possible magnetic scattering at the surface," Applied Physics Letters **92**, 212505 (2008).

[54] Jian Wei, Goutam Sheet, and Venkat Chandrasekhar, "Possible microscopic origin of large broadening param-

eter in point Andreev reflection spectroscopy," Applied Physics Letters **97**, 062507 (2010).

[55] Anne-Marie Valente-Feliciano, *Development of SRF thin film materials for monolayer/multilayer approach to increase the performance of SRF accelerating structures beyond bulk Nb*, Ph.D. thesis, University of Paris (2014).

[56] Pashupati Dhakal, Santosh Chetri, Shreyas Balachandran, Peter J. Lee, and Gianluigi Ciovati, "Effect of low temperature baking in nitrogen on the performance of a niobium superconducting radio frequency cavity," Phys. Rev. Accel. Beams **21**, 032001 (2018).

[57] S. Wilde, R. Valizadeh, O. B. Malyshev, G. B. G. Stenning, T. Sian, and B. Chesca, "Dc magnetometry of niobium thin film superconductors deposited using high power impulse magnetron sputtering," Phys. Rev. Accel. Beams **21**, 073101 (2018).